

# Modeling of a MeV-scale Particle Detector Based on Organic Liquid Scintillator

Yu.M. Malyshev<sup>\*1,2</sup>, A.M. Gangapshev<sup>1,3</sup>, V.N. Gavrin<sup>1</sup>, T.V. Ibragimova<sup>1</sup>,  
M.M. Kochkarov<sup>1</sup>, V.V. Kazalov<sup>1</sup>, D.Yu. Kudrin<sup>1</sup>, V.V. Kuzminov<sup>1,3</sup>,  
B.K. Lubsandorzhev<sup>1</sup>, G.Ya. Novikova<sup>1</sup>, V.B. Petkov<sup>1,4</sup>, A.Yu. Sidorenkov<sup>1</sup>,  
N.A. Ushakov<sup>1</sup>, E.P. Veretenkin<sup>1</sup>, D.M. Voronin<sup>1</sup>, and E.A. Yanovich<sup>1</sup>

<sup>1</sup>Institute for Nuclear Research RAS, Russia

<sup>2</sup>National Institute of Nuclear Physics, Section of Roma Tre, Italy

<sup>3</sup>Kabardino-Balkarian State University, Russia

<sup>4</sup>Institute of Astronomy RAS, Russia

September 10, 2019

## Abstract

The detectors based on the liquid scintillator (LS) monitored by an array of photo-multiplier tubes (PMT) are often used in low energy experiments such as neutrino oscillation studies and search for dark matter. Detectors of this kind operate in an energy range spanning from hundreds of keV to a few GeV providing a few percent resolution at energies above 1 MeV and allowing to observe fine spectral features. This article gives a brief overview of relevant physical processes and introduces a new universal simulation tool LSMC (Liquid Scintillator Monte Carlo) for simulation of LS-based detectors equipped with PMT arrays. This tool is based on the Geant4 framework and provides supplementing functionality for ease of configuration and comprehensive output. The usage of LSMC is illustrated by modeling and optimization of a compact detector prototype currently being built at Baksan Neutrino Observatory.

## Contents

<b>1</b>	<b>Introduction</b>	<b>2</b>	4.3	LS and PMT configuration . . .	6
<b>2</b>	<b>Light production and detection in liquid scintillators</b>	<b>2</b>	4.3.1	Geometrical configuration	6
2.1	Scintillators . . . . .	2	4.3.2	Detector response structure . . . . .	7
2.2	Photosensors . . . . .	3	4.3.3	Absorption channels . . .	7
<b>3</b>	<b>LSMC</b>	<b>4</b>	4.3.4	Concentrators . . . . .	8
3.1	LSMC introduction . . . . .	4	<b>5</b>	<b>Conclusions</b>	<b>9</b>
3.2	Input . . . . .	4	<b>6</b>	<b>Acknowledgements</b>	<b>9</b>
3.3	Output . . . . .	5	<b>Appendices</b> <b>13</b>		
3.4	Benchmarking with Daya Bay detector . . . . .	5	<b>Appendix A Example of input macro file for LSMC</b> <b>13</b>		
<b>4</b>	<b>Geo-neutrino detector prototype</b>	<b>5</b>	<b>Appendix B Output structure of LSMC</b> <b>14</b>		
4.1	Baseline prototype geometry . .	6			
4.2	Modeling with LSMC . . . . .	6			

\* Corresponding author: malyshev@inr.ru

# 1 Introduction

Construction of new large neutrino detectors is necessary for solving a number of problems of modern neutrino physics, astrophysics and geophysics. In the past, large-volume unsegmented detectors have already demonstrated their capabilities, however, larger target masses, of kiloton scale, are needed for new generation experiments in order to compensate the low strength of neutrino interactions and provide enough statistical significance of results.

A number of particle detection methods has been developed and different working substances were used as target. The organic liquid scintillators (LS), along with water, are the most suitable working substances to construct kiloton-scale neutrino detectors. In contrast to water Cherenkov detectors scintillation detectors are capable to reach energies down to hundreds keV, and thereby allow to detect, for example, geo-neutrinos and solar neutrinos from CNO cycle of sub-MeV energies.

The scintillation technique is common for an entire class of detectors which are now working in the field of neutrino physics, astrophysics and geophysics (KamLAND [1], Daya Bay [2], Double Chooz [3], RENO [4], Borexino [5] and others). Double Chooz, Daya Bay and RENO have discovered the non-zero value of the  $\theta_{13}$  oscillation parameter and Daya Bay later provided its most accurate estimate. KamLAND and Borexino have found the first evidence for the weak geo-neutrino signal originating from radioactive elements embedded in the Earth's crust.

The techniques developed for these experiments keep improving and will be used for a number of new LS-based detectors being actively planned (LENA [6], Theia [7]) and already being constructed (JUNO [8], Jinping [9]) along with existing facilities being upgraded (SNO+ [10], RENO-50 [11]). A new large-volume scintillation detector at the Baksan Neutrino Observatory for purposes of neutrino geo- and astrophysics has been discussed for a long time. Recently resumed R&D activities are aimed at the creation of such a detector [12]. A small scale prototype is already under construction.

Computer modeling of LS-based detectors plays an important role in their designing, understanding of their operation and event recon-

struction. One can use an empirical model giving a prediction of the observed energy based on initial energy, energy deposition in the scintillating volume and position of scintillation [13]. This approach requires a number of assumptions such as Gaussian distribution of detector response and small contribution of Cherenkov light. However, the assumptions made in [13] often hold in practice. We should also note that the determination of deposited energy sometimes requires a dedicated simulation.

In practice Monte Carlo (MC) simulations are usually used for this task giving more flexibility at a price of heavier computations. Simple approximated approaches are used along with more comprehensive computer programs often based on existing frameworks. In any case developing of such a tool takes significant effort and time. Future experiments may benefit from using a universal MC tool having enough flexibility and functionality.

Such a tool called LSMC (Liquid Scintillator Monte Carlo) has been created with the aim to help quickly start simulations. It is developed on top of the Geant4 toolkit [14, 15] inheriting its physical models, functionality and philosophy. It is designed to be configurable for a wide range of detector geometries, materials and PMT models with no need of any coding. Instead it is fully controlled via interactive commands or macro files. Another goal of this project is to improve existing models based on the experience gained in real applications, e.g. with the upcoming data from the detector prototype in Baksan.

An overview of the relevant physical processes and detection techniques is given in Section 2. Section 3 describes the LSMC tool and its validation. Section 4 gives an example of LSMC application for detector design. Finally, in Section 5, we summarize our results and present our conclusions.

## 2 Light production and detection in liquid scintillators

### 2.1 Scintillators

Organic liquid scintillators consist of a solvent medium and a small amount of fluor, often with an addition of a tiny amount of wavelength

shifter. The kinetic energy of charged particles crossing the medium is mainly deposited in the solvent and excites its molecules. The excitation energy is rapidly transferred to the fluor, usually by a non-radiative dipole-dipole interaction. If the emission spectrum of a fluor has a significant overlap with its own absorption spectrum or the one of the solvent, a wavelength shifter is needed for re-emission to a higher wavelength region.

The choice of a specific LS mixture depends on the physics goals and the technical design of the detector. The scintillator performance is usually optimized by maximizing its light yield, absorption and scattering lengths, and minimizing its scintillation decay time. Besides that, the emission spectrum should be in the region of the maximal sensitivity of the photomultiplier tubes (PMTs). It makes a direct impact on the detector performance, i.e. the energy and time resolution, and the low energy threshold.

Often the neutrino signal can not dominate the background even if the target mass is extremely large. When this is the case, the low-background conditions become crucial and “active” background suppression is to be used, e.g. event selection based on fast coincidences, rejection of events from the outer part of detector (fiducialization), time veto after energetic muon passing the detector, discrimination of particle type by different emission time profile (pulse shape discrimination) and others. The final effectiveness of background suppression depends on a number of LS features such as the light yield, the fluorescence time profile, the transparency and the radiopurity. These quantities are mainly defined by the purity of the original materials, as well as by temperature and aging effects.

The light yield of LS depends greatly on the concentration of fluor(s) added to the solvent, increasing at low concentrations and then saturating at a certain level. So, the optimization of the amount of collected light with regard to the self-absorption effects is needed for each specific LS mixture.

In the last decades large progress has been made in the study of the properties of different LS mixtures. At present linear alkylbenzene (LAB) is one of the most popular solvents used to produce LS for large-scale detectors. Development of a large scintillation detector requires to consider also its cost and safety. In this re-

spect, a scintillator on the basis of LAB has indisputable advantages, such as hypotoxicity, low volatility, and high flash point. Besides, LAB is a low-cost compound produced by the industry in large amounts.

## 2.2 Photosensors

Photomultiplier tubes (PMTs) are the most commonly used photon detectors in nuclear and particle physics experiments, in particular in astroparticle experiments. For large-scale LS detectors the use of large area PMTs is a must in order to collect as much light as possible, while smaller detectors can be equipped with silicon photo-multipliers (SiPM). Here only the former ones are considered.

In PMTs an individual photon can be registered via an electron produced by the photoelectric effect taking place in its front surface (photo-cathode) and then captured by electromagnetic field and amplified by a cascade of dynodes to a microscopic pulse. PMT performance affects the main parameters of the whole detector. For instance, the PMT sensitivity to scintillation light largely defines the sensitivity of LS detector as a whole. The other parameters of PMTs such as single photo-electron response, timing, dark current as well as the stability of these parameters are of crucial importance too.

The sensitivity of PMTs is characterized by photon detection efficiency (PDE). This parameter is a product of quantum efficiency of PMT’s photo-cathode (QE), collection efficiency of photo-electrons (CE) and probability to detect photo-electron by PMT’s dynode system (PD):

$$\text{PDE} = \text{QE}(\lambda) \times \text{CE}(\theta) \times \text{PD}(V), \quad (1)$$

where QE depends on photon wave-length  $\lambda$ , CE depends on incident azimuthal position  $\theta$  and PD depends on photo-cathode to first dynode voltage  $V$ .

Modern large area PMTs have high quantum efficiency, e.g. the so-called super-bialkali photo-cathodes allow to reach PDE of more than 35% at wavelengths of 360–400 nm. On top of that they have good single photo-electron response: the typical resolution of the single photo-electron peak in their photo-electron ADC charge distribution is 30-40% at gain of  $10^6$ – $10^7$ . This peak is clearly separated from the pedestal at lower ADC chan-

nels with peak-to-value ratio of more than 2.5–3. The better single photo-electron response, the higher value of PD. For modern large area PMTs the value of PD is close to 100%.

PMTs register noise pulses, known as dark current, present even in complete darkness. It is described by the dark current counting rate above certain threshold which is usually set to a fraction of single photo-electron, e.g. a quarter of mean value of photo-electron charge (0.25 p.e.). Typical values for dark current counting rate of large area PMTs are of the order of 10 kHz at room temperature.

PMT timing is characterized by single photo-electrons transit time spread (TTS or jitter). Typical values of TTS of large PMTs are in the range of 3–5 ns (FWHM). One should take into account other effects coming from the coupled electronics and distorting PMT pulse shape.

## 3 LSMC

### 3.1 LSMC introduction

A dedicated software called Liquid Scintillator Monte Carlo (LSMC) has been developed for modeling of detectors based on LS and equipped with PMT arrays. LSMC is based on the Geant4 toolkit [14, 15] utilizing its physical models, user interface and visualization functionality.

LSMC is designed to provide a user an easy way to configure own detector parameters for simulation via interactive commands or by usage of macro files, and allows to configure a variety of setups with no need to alter the code. A typical detector like the ones considered in Sections 3.4 and 4.1 is defined by  $\sim 100$  commands. In contrast, building an application using pure Geant4 would require an implementation of many objects using C++ classes provided in the package.

For the event generator LSMC utilizes Geant4 General Particle Source [16], which provides a rich functionality for setting primary particle source: particle type, energy, position, angular distributions etc.

All the standard Geant4 materials [17] are available in LSMC. Some other materials often used in construction of LS-based detectors, such as different scintillators, acrylic and mineral oil, are additionally implemented in LSMC.

Light emission is modeled with the Geant4 optical physics models (see “ElectromagneticInteractions/Optical Photons” in [18]). LS material emits photons according to a pre-defined or a user-defined scintillation yield and spectrum. The simulation includes quenching described by the Birks’ law [19] and production of Cherenkov light [20]. Although only a tiny fraction of photons in the region of PMT sensitivity is produced by Cherenkov effect, it makes an impact on the detector response non-linearity and is enabled in LSMC by default.

Photons reaching PMT photo-cathode are counted with the probability defined by the QE curve. Different simple PMT shapes are available in LSMC: cylinder, half-sphere and “bulb” (cylinder + sphere). The sizes can be set by user. Besides that LSMC provides three realistic PMT models with their QE curves: ETL-9351, Hamamatsu R5912 and Hamamatsu R7081-100. Optionally, a user can define own QE curves. The list of available PMT models is to be extended in future.

Dark noise, gain fluctuations and other PMT processes are not modeled by LSMC and may be implemented in the future updates. At the moment they can be applied manually on top of the LSMC output.

LSMC is to be publicly released in near future. However, it can be shared privately upon request. Interested groups are invited to contact the corresponding author.

### 3.2 Input

LSMC follows the concept of hierarchical organization of commands utilized in Geant4. The commands can be typed in interactive mode or written sequentially in macro files. The top level branches are responsible for configuration of event generator, physical processes, geometry, material, level of details for the output, visualization, as well as for run control. Most of them are the standard Geant4 commands. An integrated help system provides a description for each command, which is a part of the Geant4 package.

A special top level branch ‘/lsmc’ is added to group the LSMC-specific commands. The LSMC-specific commands include configuration of sizes and materials of the outer tank, the vessel for scintillator and auxiliary components. For the scintillator one can set the light output and the value of the Birks’ constant.

Special commands are available for choosing PMT type, optionally provide a specific QE curve, and define PMT arrangement.

An example of an input macro file is provided in A.

### 3.3 Output

The output of simulation is saved to a ROOT file [21]. The output data includes true event generator information (initial energy, position and momentum), energy deposition in different detector components, total number of photons, number of registered photo-electrons, number of fired PMTs, number of absorbed photons in detector components, and other information. One can also enable the extended output mode, which triggers storage of information about each registered photo-electron, such as PMT ID, generation and absorption channel and photo-cathode hit time.

See B for the full output description.

### 3.4 Benchmarking with Daya Bay detector

For verification of the correctness of the simulations performed by LSMC a benchmarked simulation has been carried out. Daya Bay detector has been chosen due to availability of published characteristics. The Daya Bay detector system [22] consists of eight identical detectors immersed into three water pools and covered by muon detectors. The eight detectors are referred to as anti-neutrino detectors (AD). Each one consists of the inner vessel with Gd-doped LAB-based LS nested in another vessel filled with undoped LS. The outer vessel and an array of 192 8-inch PMTs (Hamamatsu R5912) are placed in a tank with mineral oil. The inner and outer vessels with LS are made of acrylic. One can refer to [22] for more details.

The scintillator light yield has been set to 9000 to match the normalization coefficient of  $\sim 170$  p.e./MeV measured in Daya Bay. The Birks' coefficient has been set to  $k_B = 0.0158$  g/cm<sup>2</sup>/MeV in accordance with [23]. The detector response non-linearity has been investigated for positrons in the energy range from 0 to 10 MeV, see Fig. 1 showing dependence of  $E_{\text{vis}}/E_{\text{dep}}$  on deposited energy  $E_{\text{dep}}$ . The visible energy  $E_{\text{vis}}$  corresponds to the detectable light and is proportional to the number of detected photo-electrons. For the case

of positrons the deposited energy  $E_{\text{dep}}$  is almost always equal to the sum of kinetic energy and the energy of two annihilation gammas:  $E_{\text{dep}} = E_{\text{kin}} + 1.022$  MeV. For the LSMC data the normalization coefficient of 168 p.e./MeV has been used. The results of LSMC simulation are compared with the corresponding non-linear energy model shown in Fig. 22 of [23] (the majority of electronics non-linearities removed).

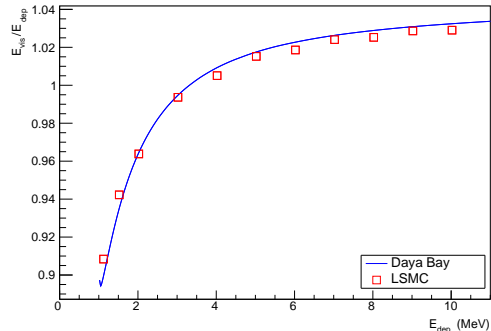


Figure 1: Daya Bay energy scale non-linearity  $E_{\text{dep}}/E_{\text{vis}}$  for positrons with the majority of electronics nonlinearity removed [24] (blue line), and the result of a LSMC simulation with manually adjusted normalization (red squares).

The agreement of the measurement-based non-linearity curve of the Daya Bay detectors with the LSMC prediction proves its reliability for simulation of similar detectors. It should be noted, however, that one has to carry out appropriate values for the scintillator light yield and Birks' constant. One should also remember about the contribution of Cherenkov light. To investigate it one can switch on and off the Cherenkov process in the simulation.

## 4 Geo-neutrino detector prototype

Baksan Neutrino Observatory in Caucasus Mountains has facilities that are among the deepest in the world. The overburden of laboratories reaches 4700 m.w.e. One of them has been used for solar neutrino monitoring by the SAGE experiment [25]. The low reactor neutrino background makes this location very promising for geo-neutrino measurements. A kiloton-scale detector has been proposed in

[26] for studies of Earth’s crust. Such a detector may reinforce the future network of geoneutrino monitors. In order to start-up this large project a small detector prototype has been designed and is currently under construction. LSMC was used at the designing stage. Some results are presented below to illustrate the functionality of LSMC.

#### 4.1 Baseline prototype geometry

The prototype has about 420 kg of LAB-based scintillator with 2,5-Diphenyloxazole (PPO) and bisMSB admixtures. The scintillator is contained within a sphere with the radius of 50 cm and varying thickness of 1-2 cm (in simulation fixed to 1 cm). The sphere is made of acrylic, a transparent material with the refraction index similar to the one of LAB. It is put into a cylindrical tank filled with water serving for protection from external radioactivity. The diameter and height of the tank are 240 and 280 cm respectively. Its dimensions are constrained by the requirement to fit the tunnel during the transportation underground.

An array of 20 10-inch Hamamatsu R7081-100 PMTs surrounds the scintillator contained in the acrylic sphere. PMTs are placed at vertices of a regular dodecahedron at about 75 cm distance measured from the sphere center to PMT equators. The PMTs and the acrylic sphere are mounted on a stainless steel supporting structure. PMTs are also to be equipped with conical concentrators in order to increase the amount of gathered light.

A realistic model of Hamamatsu R7081-100 tubes implemented in LSMC was used for this simulation. Its shape and dimensions taken from the manufacturer’s data sheets are shown in Fig. 2.

#### 4.2 Modeling with LSMC

The prototype has been modeled with the LSMC software in order to better understand the light absorption budget, impact of different geometry choices on light collection, and other aspects prior to the construction. In all simulations primary electrons with total energy of 1 MeV were generated uniformly over the entire liquid scintillator volume with isotropic directionality. Some smaller parts of the detector structures (like PMT holding structures, cables etc.) were omitted for simplicity.

### 4.3 LS and PMT configuration

The exact light yield of LAB and fluor concentrations are not determined yet, therefore an conservative estimate of 10000 photons/MeV (as in [13] and in [27]) and an approximate emission spectrum are used for simulations. The emission spectrum is shown on the upper panel of Fig. 3 together with the QE curve of the photo-multiplier tubes to be used for the detector. The bottom panel of Fig. 3 illustrates LAB and water absorption spectra used in simulation. More details on light emission and absorption in LAB-based scintillators can be found in [27]. Here we used similar spectra. The absorption length of water can vary in a wide range depending on the level of purification: from several meters for “tap” water to a few hundreds of meters for “ultra-pure” water [28, 29, 30]. Water transparency is not of crucial importance in our case due to the array size and we chose reasonable values from [31, 32] which could be reached easily for affordable price.

#### 4.3.1 Geometrical configuration

The two most natural and commonly used geometry choices for LS vessel are cylinder and sphere. The first one is easier to fabricate, the other one provides better symmetry, which in turn simplifies energy reconstruction. Here we compare the two options assuming the same LS mass of about 420 kg. The sphere has the inner radius of 49 cm, and the cylinder has the inner radius of 42.8 cm and the height of 85.6 cm. These two options are considered below in combination with two PMT arrangement configurations: cylindrical and spherical, see Fig. 4 for illustration.

Fig. 5 shows detector response in terms of number of registered photo-electrons for the three introduced combinations. In case of the “shp.-sph.” configuration (with spherical LS volume and spherical PMT arrangement) it consists of a peak with a shoulder. However, as it will be discussed later, the events contributing to the shoulder can be easily separated from the ones from the main peak. Thus, after event reconstruction, this feature will not spoil the final energy resolution.

The “cyl.-cyl.” configuration provides slightly better light collection than the other options, but the peak smearing is a bit larger compared to the main peak of the “sph.-sph.”

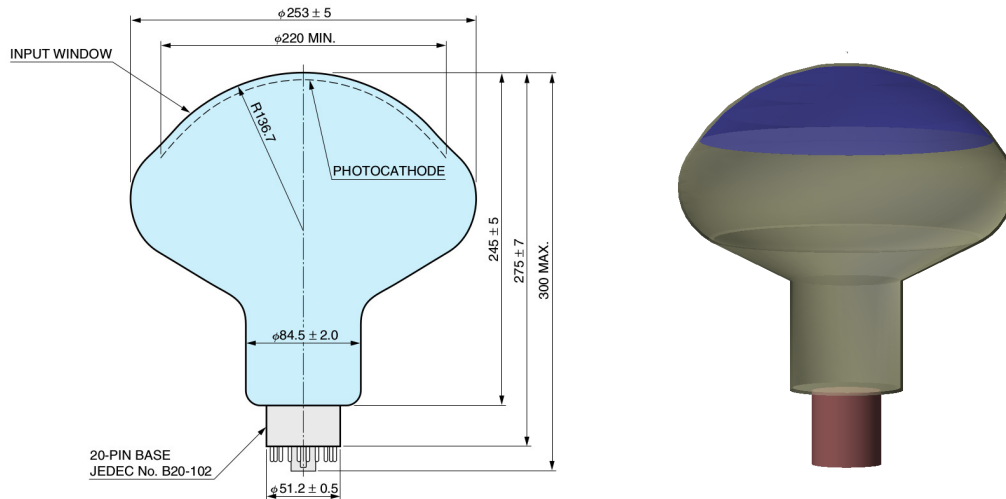


Figure 2: Hamamatsu R7081 PMT geometry: from Hamamatsu data sheets (left), LSMC model (right).

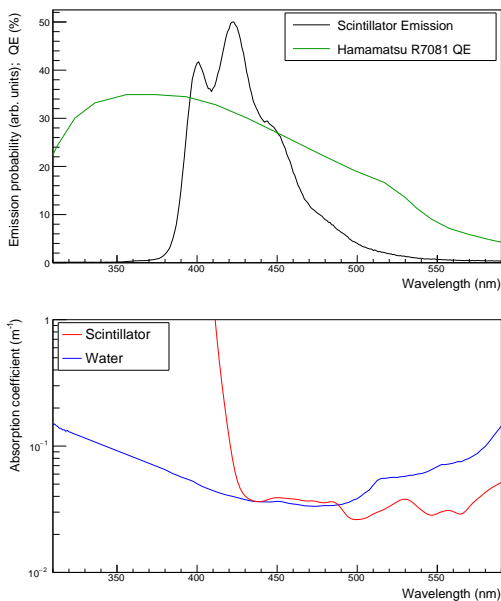


Figure 3: *Top panel:* Light emission curve (including re-emission) of LAB scintillation and PMT QE in LSMC. *Bottom panel:* light absorption spectra for LAB-based scintillator and water in LSMC. The emission and absorbance data are taken from [33]; PMT QE curve is from Hamamatsu data sheets.

option. The mixed configuration with spherical LS volume and cylindrical PMT arrangement (“sph.-cyl”) inherits the drawbacks of both other and, therefore, is the least favor-

able. The “sph.-sph.” option has been selected for the discussed here detector prototype and is considered below as the default.

#### 4.3.2 Detector response structure

The photo-electron spectrum for the baseline configuration is shown in Fig. 6. The main peak corresponds to the events originating from the inner part of the scintillator sphere, while the smaller one is formed by the events from the outer zone. The red and blue lines show the corresponding contributions. Photons emitted in vicinity of the acrylic sphere ( $R > 46$  cm in our case) may have the angle of incidence larger than the critical one when they reach the acrylic-water boundary. These photons are reflected back to the LS volume. Within a spherical volume they have the same angle of incidence when they reach acrylic boundary again (neglecting scattering), and can never penetrate to water. This portion of photons is not detected and such events with partially lost luminosity form the smaller peak of the response spectrum.

#### 4.3.3 Absorption channels

Table 1 shows the photon absorption budget for the baseline configuration and two modified detector configurations: 1) with black inner surface of the outer tank and 2) with light concentrators mounted on PMTs. In particu-

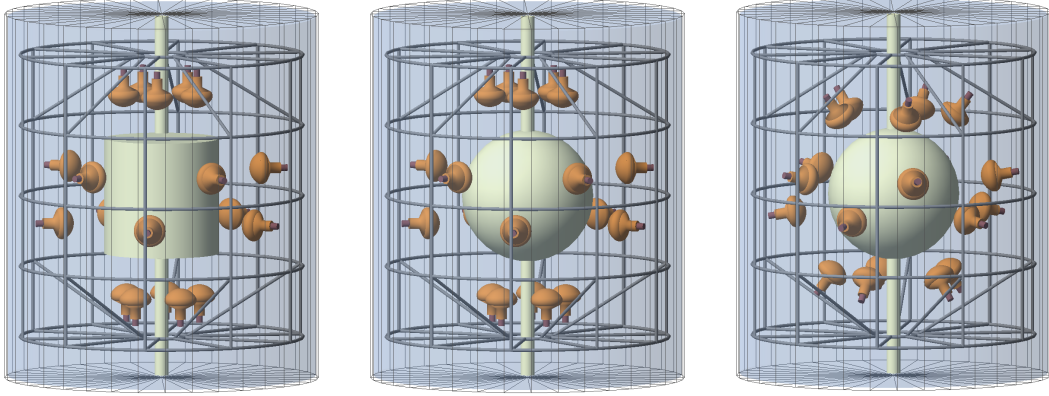


Figure 4: Different PMT arrangement options from left to right: 1) cylindrical LS volume, cylindrical PMT arrangement (“cyl.-cyl.”), 2) spherical LS volume, cylindrical PMT arrangement (“sph.-cyl.”), 3) spherical LS volume, spherical PMT arrangement (“sph.-sph.”).

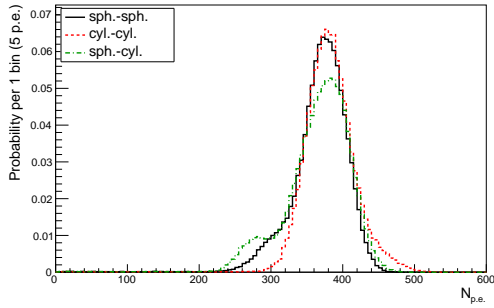


Figure 5: Detector response to 1 MeV electrons uniformly distributed over the LS volume for three arrangement options.

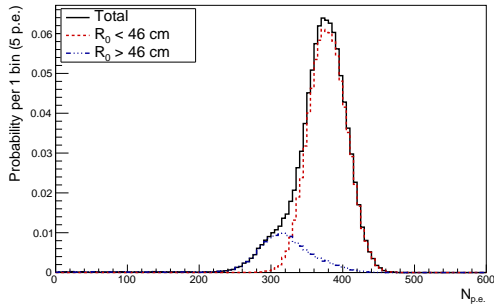


Figure 6: Detector response to 1 MeV electrons uniformly distributed over the LS volume. Contributions of the events originating from  $R_0 < 46$  cm and  $R_0 > 46$  cm are shown by red and blue lines respectively.

lar one can see that the most of the light is

absorbed by LS, so even for such a small detector as considered here the LS transparency plays an important role.

The default reflectivity of the water tank inner surface is 85%, and a non-negligible fraction of light can be reflected, and then reach a PMT photo-cathode. From one side the reflected photons increase the overall light collection. From the other side they have longer paths, which leads to additional stochastic effects and spoils the energy resolution. One can consider the inner surface of the water tank having zero reflectivity. In this case (see 3rd column of Table 1) the amount of light absorbed on its inner surface increases by factor of about 2.7 with respect to the default configuration. As the result the total light collection (absorption on photo-cathode) decreases by a factor of about 1.7. Fig. 7 shows a comparison of photo-electron spectra with 85% (default) and 0% reflectivity of the tank inner surface.

The other components, mainly supporting structures, may also play an important role in the photon collection budget. They are considered here totally non-reflecting and absorb from 6% to 23% of photons in the considered configurations.

#### 4.3.4 Concentrators

The light collection efficiency can be increased by equipping PMTs with concentrators. This idea has been already used in other neutrino detectors, e.g. in Borexino [34]. For the best performance the shape of the concentrators



Table 1: Share of absorption channels given in percents for the baseline setup, and for two modified configurations.

Absorbing material	Baseline configuration	Baseline with black tank	Baseline with concentrators
Scintillator	35	33	36
Acrylic sphere	4	3	5
Water	8	3	7
Tank	18	49	12
PMT glass and coating	0.1	<0.1	0.1
Photo-cathode	12	7	20
Other components	23	6	20

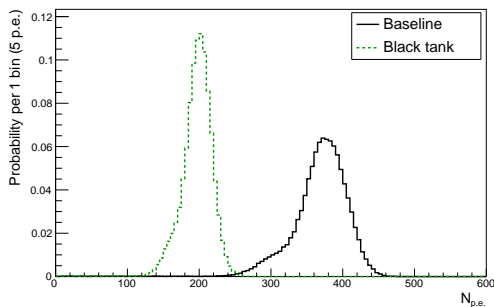


Figure 7: Detector response to 1 MeV electrons uniformly distributed over the LS volume for 85% (baseline) and 0% (black tank) reflectivity of the inner surface of the water tank.

must be properly calculated. Here for simplicity we consider truncated cone shape, see the right side of Fig. 8 for illustration. We optimized the cone dimensions using LSMC simulation, however understanding its limitation. Assuming that the larger radius must be as large as possible to capture more light, and the smaller one must coincide with the photo-cathode edge, the only parameter for optimization is the height of the truncated cone.

A set of calculations with different concentrator heights has been performed in order to find the optimal one. The corresponding response functions for some of them are shown in Fig. 8. The one with the height of 10 cm provides the best performance in terms of resolution. Therefore, we conclude that the concentrators used for the prototype should have a height of about 9–11 cm. The corresponding photon absorption budget (for the concentrator height of 10 cm) is presented in the 4th column of Table 1.

## 5 Conclusions

Modern simulation techniques allow us to construct realistic models and perform fine tuning for detectors at the early designing stage. One can learn a lot about the impact of different geometry and material choices from such simulations. Existing general purpose software and libraries are available but significant effort is still needed to develop a ready to use computer program for a particular use case. Specialized tools for specific detector classes may help to start simulations quicker.

Introduced here LSMC software allows to model LS-based detectors with no need of coding, while offering a rich functionality. It includes geometry and material configuration, type of PMTs and different ways of their arrangement. LSMC provides a large set of output information in the widely used ROOT-format.

LSMC uses the state-of-the-art libraries for physical processes from the Geant4 package. Thus, any updates in new versions of Geant4 automatically propagate to LSMC. From the other side real data measured and benchmarked with LSMC (e.g. from the new detector prototype at Baksan) may help to spot any problems, especially for the optical processes, and provide a useful input for the Geant4 developers and users.

## 6 Acknowledgements

The simulated detector prototype configuration is based on the scientific equipment of UNU GGNT BNO INR RAS partially acquired with financial support of the Ministry of Science and Higher Education of the Russian Federation: agreement N 14.619.21.0009, unique

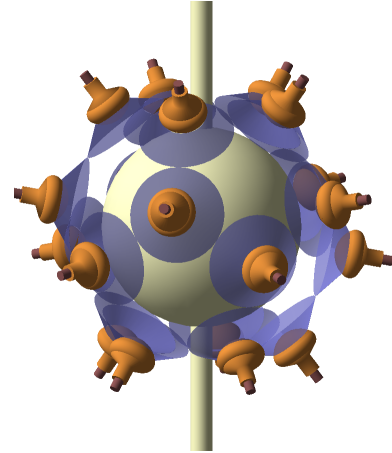
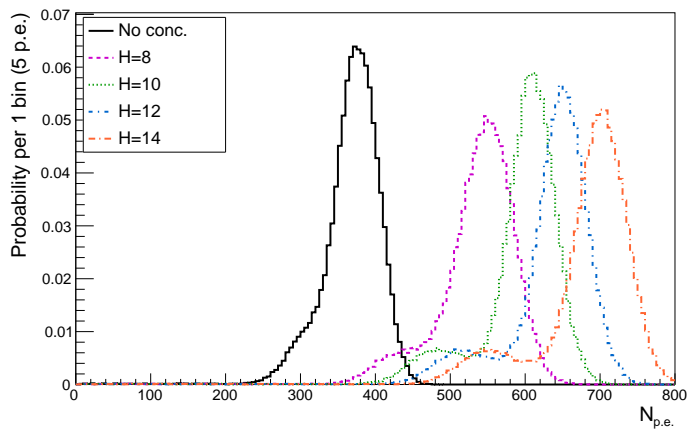


Figure 8: Light concentrators of 11 cm height mounted on PMTs (right side) and response functions for concentrators of 8, 10, 12 and 14 cm height shown by color lines. Detector response with no concentrator is shown by black line for comparison.

identifier of the project RFMEFI61917X0009.

The work was supported by the Russian Science Foundation, project no. 17-12-01331.

## References

- [1] K. Eguchi, et al., First results from KamLAND: Evidence for reactor anti-neutrino disappearance, *Physical Review Letters* 90 (2003) 021802. doi:10.1103/PhysRevLett.90.021802.
- [2] D. Adey, et al., Measurement of electron antineutrino oscillation with 1958 days of operation at Daya Bay, *Physical Review Letters* 121 (24) (2018) 241805. doi:10.1103/PhysRevLett.121.241805.
- [3] Y. Abe, et al., Indication of reactor  $\bar{\nu}_e$  disappearance in the Double Chooz experiment, *Physical Review Letters* 108 (2012) 131801. doi:10.1103/PhysRevLett.108.131801.
- [4] G. Bak, et al., Measurement of reactor antineutrino oscillation amplitude and frequency at RENO, *Physical Review Letters* 121 (2018) 201801. doi:10.1103/PhysRevLett.121.201801.
- [5] M. Agostini, et al., Spectroscopy of geoneutrinos from 2056 days of Borexino data, *Physical Review D* 92 (2015) 031101. doi:10.1103/PhysRevD.92.031101.
- [6] M. Wurm, et al., The next-generation liquid-scintillator neutrino observatory LENA, *Astroparticle Physics* 35 (11) (2012) 685–732. doi:10.1016/j.astropartphys.2012.02.011.
- [7] V. Fischer, Theia: A multi-purpose water-based liquid scintillator detector, in: 13th Conference on the Intersections of Particle and Nuclear Physics (CIPANP 2018), 2018. arXiv:1809.05987.
- [8] F. An, et al., Neutrino Physics with JUNO, *Journal of Physics G* 43 (3) (2016) 030401. doi:10.1088/0954-3899/43/3/030401.
- [9] J. F. Beacom, et al.
- [10] S. Andringa, et al., Current Status and Future Prospects of the SNO+ Experiment, *Advances in High Energy Physics* 2016 (2016) 6194250. doi:10.1155/2016/6194250.
- [11] H. Seo, Status of RENO-50, *Proceedings of Science NEUTEL2015* (2015) 083. doi:10.22323/1.244.0083.
- [12] I. Barabanov, et al., Large-volume detector at the Baksan Neutrino Observatory for studies of natural neutrino fluxes for purposes of geo- and astrophysics, *Physics of Atomic Nuclei* 80 (2017) 446. doi:10.1134/S1063778817030036.
- [13] L. Lebanowski, L. Wan, X. Ji, Z. Wang, S. Chen, An efficient energy response model for liquid scintillator detectors, *Nuclear Instruments and Methods A* 890 (2018) 133 – 141. doi:10.1016/j.nima.2018.02.077.
- [14] S. Agostinelli, et al., Geant4: a simulation toolkit, *Nuclear Instruments and Methods A* 506 (3) (2003) 250–303. doi:10.1016/S0168-9002(03)01368-8.
- [15] J. Allison, et al., Geant4 developments and applications, *IEEE Transactions on Nuclear Science* 53 (1) (2006) 270. doi:10.1109/TNS.2006.869826.
- [16] Geant4 General Particle Source, available at <http://geant4-userdoc.web.cern.ch/geant4-userdoc/UsersGuides/ForApplicationDeveloper/html/GettingStarted/generalParticleSource.html>.
- [17] Geant4 Material Database, available at <http://geant4-userdoc.web.cern.ch/geant4-userdoc/UsersGuides/ForApplicationDeveloper/html/Appendix/materialNames.html>.
- [18] Geant4 Physics Reference Manual, available at <http://geant4-userdoc.web.cern.ch/geant4-userdoc/UsersGuides/PhysicsReferenceManual/html/index.html>.

- [19] J. Birks, Scintillations from organic crystals: Specific fluorescence and relative response to different radiations, *Proc. of the Phys. Soc., Section A* 64 (10) (1951) 874–877. doi:10.1088/0370-1298/64/10/303.
- [20] P. Cherenkov, Visible luminescence of pure liquids under the influence of gamma-radiation, *Usp. Fiz. Nauk* 93, no.2 (1967) 385. doi:10.3367/UFNr.0093.196710n.0385.
- [21] R. Brun, F. Rademakers, ROOT: An object oriented data analysis framework, *Nuclear Instruments and Methods A* 389 (1997) 81–86. doi:10.1016/S0168-9002(97)00048-X.
- [22] F. An, et al., The detector system of the daya bay reactor neutrino experiment, *Nuclear Instruments and Methods A* 811 (2016) 133 – 161. doi:https://doi.org/10.1016/j.nima.2015.11.144.
- [23] D. Adey, et al., A high precision calibration of the nonlinear energy response at daya bay, *Nuclear Instruments and Methods A* 940 (2019) 230 – 242. doi:https://doi.org/10.1016/j.nima.2019.06.031.
- [24] Y. Huang, "Data for: A high precision calibration of the nonlinear energy response at Daya Bay", *Mendeley Data*, v1 (2019). doi:http://dx.doi.org/10.17632/2jv89c92ff.1.
- [25] J. N. Abdurashitov, et al., Measurement of the solar neutrino capture rate with gallium metal. III. Results for the 2002–2007 data-taking period, *Physical Review C* 80 (2009) 015807. doi:10.1103/PhysRevC.80.015807.
- [26] G. Domogatski, V. Kopeikin, L. Mikaelyan, V. Sinev, Neutrino geophysics at Baksan I: Possible detection of georeactor anti-neutrinos, *Physics of Atomic Nuclei* 68 (2005) 69–72, [*Yad. Fiz.*68,70(2005)]. doi:10.1134/1.1858559.
- [27] H.-L. Xiao, L. Xiao-Bo, D. Zheng, J. Cao, L.-J. Wen, N.-Y. Wang, Study of absorption and re-emission processes in a ternary liquid scintillator system, *Chinese Physics C* 34 (11) (2010) 1724–1728. doi:10.1088/1674-1137/34/11/011.
- [28] K. Abe, et al., Calibration of the Super-Kamiokande Detector, *Nuclear Instruments and Methods A* 737 (2014) 253,272. doi:10.1016/j.nima.2013.11.081.
- [29] F. Sogandares, E. Fry, Absorption spectrum (340-640 nm) of pure water. I. Photothermal measurements, *Applied Optics* 36 (1997) 8699–8709. doi:10.1364/AO.36.008699.
- [30] R. Pope, E. Fry, Absorption spectrum (380-700 nm) of pure water. II. Integrating cavity measurements, *Applied Optics* 36 (1997) 8710–8323. doi:10.1364/AO.36.008710.
- [31] C. Mobley, The optical properties of water in *Handbook of Optics*, McGraw-Hill Education, New York, 1995, pp. 43.3–43.56.
- [32] M. Querry, D. Wieliczka, D. Segelstein, Water (H<sub>2</sub>O) in *Handbook of Optical Constants of Solids II*, Academic, San Diego, California, 1991, pp. 1059–1077.
- [33] W. Beriguete, et al., Production of gadolinium-loaded liquid scintillator for the daya bay reactor neutrino experiment, *Nuclear Instruments and Methods A* 763. doi:10.1016/j.nima.2014.05.119.
- [34] L. Oberauer, C. Grieb, F. von Feilitzsch, I. Manno, Light concentrators for Borexino and CTF, *Nuclear Instruments and Methods A* 530 (2004) 453462. doi:10.1016/j.nima.2004.05.095.

# Appendices

## Appendix A Example of input macro file for LSMC

An example of simulation configuration (for Baksan prototype):

```
-----  
# PMT configuration  
/lsmc/pmt/type R7081-100  
/lsmc/pmt/shape R7081  
#  
# PMT arrangement  
#           R   theta   N phi0  
/lsmc/pmt/addRingRTheta 79 37.3758 5 18  
/lsmc/pmt/addRingRTheta 79 79.1874 5 18  
/lsmc/pmt/addRingRTheta 79 100.8126 5 54  
/lsmc/pmt/addRingRTheta 79 142.6242 5 54  
#  
# Concentrators  
/lsmc/enableConc 24.4 11.0 # R H (in cm)>  
#  
# Scintillator  
/lsmc/scint/material LAB  
/lsmc/scint/shape sphere  
/lsmc/scint/radius 49. cm  
/lsmc/scint/holderThickness 2. cm  
/lsmc/scint/holderMaterial Acrylic  
/lsmc/scint/yield 10000  
#  
# Inner vessel configuration  
/lsmc/tank/radius 120 cm  
/lsmc/tank/height 280 cm  
/lsmc/tank/thickness 2.0 cm  
/lsmc/tank/reflectivity 0.85  
/lsmc/tank/fillingMaterial Water  
#  
# Additional structures  
# LS tubes  
/lsmc/misc/addTube ls_tube 4.5 5.5 Acrylic 0 0 49 0 0 140  
/lsmc/misc/addTube ls_tube 4.5 5.5 Acrylic 0 0 -49 0 0 -140  
# vertical tubes           x1  y1  z1      x2  y2  z2  
/lsmc/misc/addTube truss 0 1.25 StainlessSteel 110 0 110 110 0 -110  
...  
# horizontal tubes, top           x1  y1  z1      x2  y2  z2  
/lsmc/misc/addTube truss 0 1.25 StainlessSteel 110 0 110 20 0 110  
...  
# horizontal tubes, bottom           x1  y1  z1      x2  y2  z2  
/lsmc/misc/addTube truss 0 1.25 StainlessSteel 110 0 -110 20 0 -110  
...  
# inclined tubes, top           x1  y1  z1      x2  y2  z2  
/lsmc/misc/addTube truss 0 1.25 StainlessSteel 89 65 55 16 12 110  
...  
# inclined tubes, bottom           x1  y1  z1      x2  y2  z2  
/lsmc/misc/addTube truss 0 1.25 StainlessSteel 89 65 -55 16 12 -110  
...  
# Ring-tubes, side  
/lsmc/misc/addTorus truss 0 1.25 110 StainlessSteel 0 0 110  
...
```

```

# Ring-tubes, top and bottom
/lsmc/misc/addTorus truss 0 1.25 20 StainlessSteel 0 0 110
/lsmc/misc/addTorus truss 0 1.25 20 StainlessSteel 0 0 -110
#
/run/initialize
#
# Primary particles
/gps/particle e-
/gps/energy 1 MeV
/gps/pos/type Volume
/gps/pos/shape Sphere
/gps/pos/radius 49 cm
/gps/ang/type iso
#
# Inactivate optical processes
# (Cerenkov, Scintillation, OpAbsorption, OpRayleigh, OpMieHG, OpBoundary, OpWLS)
#/process/inactivate Cerenkov
#/process/inactivate OpAbsorption
#/process/inactivate OpRayleigh
#
/run/printProgress 5000
/run/beamOn 100000

```

Symbol '#' stands for comments, the lines starting with this character are ignored by LSMC. To explore all the commands and descriptions one can run './LSMC' and type 'help', then walk through the menu to see all the options.

## Appendix B Output structure of LSMC

The LSMC output is stored in ROOT format [21] and has two modes: normal and extended. The later one additionally includes photon-wise info and can be enabled by command `/lsmc/recPhotonInfo True`. The data structure is the following (the data fields marked with "\*" are only available in the extended output mode):

Data type	Field name	Description
TTree	pmt_pos	List of PMT positions in the detector. Index number in the list corresponds to its ID.
	pmtX_cm, pmtY_cm, pmtZ_cm	x-, y- and z-coordinate of PMT.
TTree	evt	Event-wise information.
	x0_cm, y0_cm, z0_cm	x-, y- and z-coordinates of event.
	E0_MeV	Primary kinetic particle energy.
	px0, py0, pz0	x-, y-, z-components of primary particle momentum normalized to 1.
	edepScint_MeV	Energy deposition in scintillator.
	edepHolder_MeV	Energy deposition in scintillator holder.
	edepWater_MeV	Energy deposition in outer tank filler.
	nPMTs	Number of fired PMTs.
	nHits[nPMTs]	Vector of hits in fired PMTs.
	fHitTime_ns[nPMTs]	Vector of first hit times in fired PMTs.
	totalPE	Total number of detected photo-electrons.
	hc_x_cm, hc_y_cm, hc_z_cm	x-, y-, and z-coordinates of hit center.
	nPhotons	Number of photons produced by scintillator.

	phEnergy_eV[nPhotons]	Vector of photon energies (*)
	phTrackLen_cm[nPhotons]	Vector of photon track lengths (*)
	phGenChannel[nPhotons]	Vector of photon generation channels (*)
	phAbsChannel[nPhotons]	Vector of photon absorption channels (*)
	phHitLocalTime_ns[nPhotons]	Vector of photon local hit times (*)
	phHitGlobalTime_ns[nPhotons]	Vector of photon global hit times (*)
	absScint	Number of photons absorbed in scintillator.
	absHolder	Number of photons absorbed in scintillator holder.
	absWater	Number of photons absorbed in outer tank filler.
	absPmtGlass	Number of photons absorbed in PMT glass.
	absPmtEnd	Number of photons absorbed in PMT end.
	absPmtCoating	Number of photons absorbed on PMT coating surface.
	absPhotocath	Number of photons absorbed in PMT photo-cathode.
	absTank	Number of photons absorbed on outer tank surface.
	absConcentr	Number of photons absorbed on concentrator surface.
TGraph	scintSpec_eV, scintSpec_nm	Scintillator emission spectrum.
TGraph	scintAbs_eV, scintAbs_nm	Scintillator absorption spectrum.
TGraph	acrylAbs_eV, acrylAbs_nm	Scintillator holder absorption spectrum.
TGraph	waterAbs_eV, waterAbs_nm	Outer tank filler absorption spectrum.
TGraph	pmtQE_eV, pmtQE_nm	PMT QE curve

---